Solitonic black holes induced by magnetic solitons in a dc-SQUID array transmission line coupled with a magnetic chain

Haruna Katayama,[1] Satoshi Ishizaka,[2] Noriyuki Hatakenaka,[2,*] and Toshiyuki Fujii[3]

[1]*Graduate School of Integrated Arts and Sciences, Hiroshima University, Higashihiroshima 739-8521, Japan*

[2]*Graduate School of Advanced Science and Engineering, Hiroshima University, Higashihiroshima 739-8521, Japan*

[3]*Department of Physics, Asahikawa Medical University, Midorigaoka-higashi, Asahikawa 078-8510, Japan*

(Received 29 November 2020; accepted 2 March 2021; published 30 March 2021)

We investigate analog black holes generated in an array of direct current superconducting quantum interference devices (dc SQUIDs) coupled in parallel with a one-dimensional chain of single-domain nanomagnets. Magnetic solitons in the chain provide magnetic fields perpendicular to the SQUID array. This leads to the spatially varying velocities of electromagnetic waves through the nonlinear inductance in the array required for creating effective event horizons, resulting in analog black holes. We derive the Hawking temperature in this analog black hole based on the tunneling mechanism for Hawking radiation. The formula reflecting the soliton properties shows that Hawking radiation is observable using the current state-of-the-art technologies.

DOI: 10.1103/PhysRevD.103.066025

I. INTRODUCTION

Hawking radiation is blackbody radiation emitted from a black hole, from which even light is believed to be unable to escape [1,2]. This occurs due to quantum-mechanical effects near the black hole event horizon. According to the uncertainty principle, virtual particle pairs are constantly being created and then quickly annihilate each other everywhere. But, near the horizon of a black hole, it is possible for one to fall in before the annihilation can happen, in which case the other one escapes as Hawking radiation. Hawking radiation is a rare example where general relativity and quantum mechanics meet. Therefore, the observation of Hawking radiation is a touchstone for the unified theory incorporating both general relativity and quantum mechanics. Unfortunately, Hawking radiation has never been observed, because the Hawking temperature is about 10^{-8} K for a solar mass black hole, which is much smaller than the cosmic background radiation temperature (3K). As a result, it is difficult to study actual black holes.

This brought us to the analog black hole scenario pioneered by Unruh in sonic systems [3]. Since then, analog black holes have been investigated in various systems such as liquid helium [4], optical fibers [5], and Bose-Einstein condensates [6]. In addition, Schützhold and Unruh proposed the analog black holes using electromagnetic transmission lines [7]. Later, Nation *et al.* extended their idea to *superconducting* transmission lines equipped with direct current superconducting interference devices (dc SQUIDs) [8]. They have overcome the main drawback in the Schützhold and Unruh system, namely, heating due to the dissipative processes that hinder observation, by using superconductors for the waveguides themselves. In addition, there are many advantages to superconducting devices, such as lithographic scalability, compatibility with high-precision microwave control due to their strong coupling and operability at nanosecond timescales.

Their proposed scheme for creating an effective event horizon is dual to the previous one. The analog event horizon occurs where the speed of analog light equals the spatially varying background flow. Note that the roles of light and the background field are reversed in the transmission line. That is, the velocity of electromagnetic waves changes spatially. The velocity of electromagnetic waves per unit length a in the transmission line is represented by $c = a/\sqrt{LC}$ with the inductance L and the capacity C of the circuit. Therefore, spatial dependence can be introduced into the velocity of electromagnetic waves through inductance or capacitance. An externally applied laser beam to the transmission line for modulating the capacitance is employed in the previous study. However, the laser-based illumination generates a large number of excess environmental photons, leading to heating problems. To avoid these unwanted dissipations, Nation *et al.* applied an external magnetic flux to the SQUID array in the form

*noriyuki@hiroshima-u.ac.jp

of a steplike *moving* flux pulse with a fixed velocity. Then they theoretically succeeded in generating the horizon where the pulse velocity is equal to the velocity of electromagnetic waves in the dc-SQUID array transmission line.

Here, we further extend their theory to an external magnetic field using magnetic solitons to create analog black hole *solitons*. The pulse current that generates the magnetic field applied to the SQUID array generally changes its shape with time due to wave number dispersion. This makes the analog event horizon unstable. To create a stable horizon, we utilize solitons that propagate stably in nonlinear dispersive systems due to their self-reinforcing nature caused by balancing nonlinear and dispersive effects [9–11]. This feature also provides an alternative platform for exploring uncharted aspects of analog black hokes like dynamical features of event horizons and quantum birth of a *micro* black hole pair.

Solitons in magnetic chains with easy-axis anisotropy are formed by the competition between the exchange energy J and the anisotropy energy D, leading to moving domain walls connecting between two different but energetically degenerate ground states [12,13]. In a ferromagnet, a π soliton mediates between the ground states of the upward and downward magnetic moments, for example. In our proposed system, magnetic solitons play a role in generating the magnetic field applied to the dc-SQUID array. Thus, single-domain magnetic nanoparticles are aligned just below the dc-SQUID transmission line indicated in Fig. 1.

The remainder of this paper is organized as follows. We begin with a description of the magnetic soliton in a single-domain magnetic nanoparticle chain that provides the external magnetic field applied to the SQUID array, which is the key issue in this paper. In particular, the alternating upward and downward magnetic moments in the chain in Fig. 1(b) are effectively treated as the magnetic moments pointing in the same direction. We consider two types of solitons that produce black holes and black hole–white hole pairs. We then describe black holes using solitons and discuss the observability of Hawking radiation in our analog black holes by assessing the Hawking temperature. The soliton characteristics appearing in the Hawking temperature formula play a critical role in the identification of Hawking radiation. The paper ends with a discussion.

II. MAGNETIC BIAS CONTROLLED BY MAGNETIC SOLITONS

A. Model

Let us consider a coplanar dc-SQUID array consisting of identical capacitance C and critical current I_c in all Josephson junctions together with a single-domain magnetic nanoparticle chain as shown in Fig. 1. As shown in Fig. 1(b), the chain composed of alternating nanosized single-domain magnets with different magnetic moment spacing $a/2$ is arranged in parallel at a distance l just below the dc-SQUID array.

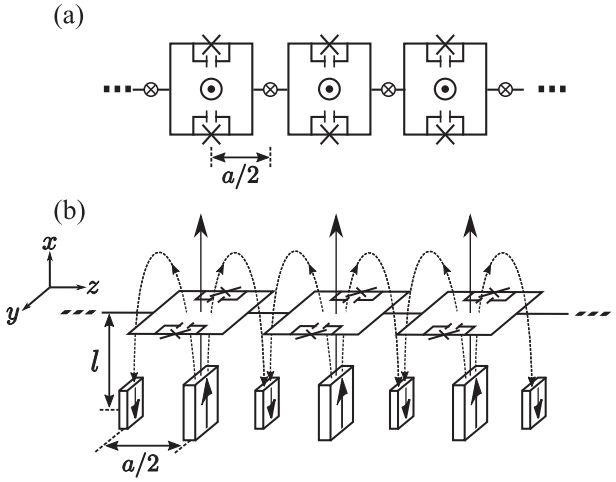

FIG. 1. (a) Diagram of a dc-SQUID array transmission line with identical capacitance C and critical current I_c in all Josephson junctions (top view). A circled dot and a cross inside the circle represent the magnetic flux applied from back to front and the opposite direction, respectively, when viewed from a vertical direction on a page. (b) Schematic diagram of our system. Nanosized single-domain magnets with magnetic moments different in size arranged below the dc-SQUID transmission line. The magnetic flux line exits from the large upward magnetic moment and enters the small downward magnetic moment.

Suppose that all of the single-domain nanoparticles have the same size. The magnetic moments in the single-domain nanoparticle chain are inevitably forced to align alternately due to the dipole-dipole interaction. Therefore, we have no choice but to use a soliton-bearing nanoparticle model with antiferromagnetic interaction [14] as a starting point. However, the single-domain nanoparticle chain with antiferromagnetic interaction results in generating a nonmagnetic field. In order to generate the suitable external magnetic field applying to the dc-SQUID array, we adopt the arrangement of single-domain nanoparticles of two sizes that alternate, in which magnetic moments alternate upward and downward similar to ferrimagnet as shown in Fig. 1(b). Hereafter, we call this chain a ferrimagnetic-aligned nanoparticle chain. In the following, we will show that a nanomagnetic material with a small magnetic moment is substantially renormalized into a nanomagnetic material with a large magnetic moment in the ferrimagnetic-aligned nanoparticle chain and can be effectively regarded as an alignment of same-sized nanoparticles similar to ferromagnets, i.e., a ferromagnetic-aligned nanoparticle chain. The system we consider is, thus, a system that introduces a magnetic field generated by a well-controllable soliton into the framework of Nation's black hole system.

B. Ferrimagnetic-aligned nanoparticle chains

The model Hamiltonian for the ferrimagnetic-aligned nanoparticle chain with different sublattice anisotropies placed just below the dc-SQUID array is represented by

$$\begin{aligned}\hat{H} = J\sum_n (\hat{S}_{2n-1}\cdot\hat{\sigma}_{2n} + \hat{\sigma}_{2n}\cdot\hat{S}_{2n+1}) \\ + \sum_n \{K_\sigma^z(\hat{\sigma}_{2n}^z)^2 - K_\sigma^x(\hat{\sigma}_{2n}^x)^2\} \\ + \sum_n \Bigg[K_S^z(\hat{S}_{2n-1}^z)^2 - K_S^x(\hat{S}_{2n-1}^x)^2 \\ - \frac{K_S^{xy}}{4}\{(\hat{S}_{2n-1}^x)^2 - (\hat{S}_{2n-1}^y)^2\}^2\Bigg],\end{aligned} \tag{1}$$

where the operators $\hat{S}_n$ and $\hat{\sigma}_n$ refer to the large and small magnetic moments of the single-domain magnets at the nth site of each sublattice, respectively. The first parenthesis on the right-hand side of Eq. (1) represents the dipole-dipole interaction energy with antiferromagnetic coupling ($J > 0$) between them. The second one represents magnetic anisotropy energy for small magnetic moments with $K_\sigma^{x(z)}(>0)$ being the magnetic anisotropy parameter of the $x(z)$ component. Similarly, the last one expresses magnetic anisotropy energy for large magnetic moments, including two types of anisotropy. One is uniaxial anisotropy with $K_S^{x(z)}(>0)$ being the anisotropy parameter of the $x(z)$ component, similar to small magnetic moments. The other is biaxial anisotropy [15] with anisotropy constant $K_S^{xy}(>0)$ coming from fourfold symmetric, which is not available in small magnetic moments. Let us assume here the relations $K_S^z \gg K_S^x, K_S^{xy}$ and $K_\sigma^z \gg K_\sigma^x$. This implies that the single-domain magnetic nanoparticle at each site has an xy easy plane. In this paper, the magnetic moment operators can be treated as classical vectors due to large magnitudes of magnetic moments in the single-domain nanoparticles; $\hat{S}_n \to \boldsymbol{S}_n = (S_n^x, S_n^y, S_n^z)$, and $\hat{\sigma}_n \to \boldsymbol{\sigma}_n = (\sigma_n^x, \sigma_n^y, \sigma_n^z)$.

C. Effective ferromagnetic-aligned nanoparticle chains

Here, we derive the effective ferromagnetic Hamiltonian from our original ferrimagnetic Hamiltonian for a single-domain ferrimagnetic-aligned nanoparticle chain by eliminating the variables $\boldsymbol{\sigma}$ for small magnetic moments [16]. This can be achieved by tracing out the relevant variables in the partition function. For the sake of simplicity, let us focus on the specific Hamiltonian $H^{(2n)}$, which is related only to $\boldsymbol{S}_{2n\pm1}$ and $\boldsymbol{\sigma}_{2n}$. By integrating the classical partition function over $\boldsymbol{\sigma}_{2n}$, the effective Hamiltonian $H'^{(2n)}$ depending only on $\boldsymbol{S}_{2n}$ is obtained as follows: The partition function is given as

$$Z = \int d\boldsymbol{\sigma}_{2n} \exp(-\beta H^{(2n)}) = \exp[-\beta H'^{(2n)}], \tag{2}$$

with inverse temperature β and the Hamiltonian $H^{(2n)}$ written as

$$H^{(2n)} = H_S^{(2n)} + H_\sigma^{(2n)} + H_{S\sigma}^{(2n)}, \tag{3}$$

where the first and second terms are Hamiltonians for large magnetic moments and small magnetic moments, respectively, and the last term is their interaction Hamiltonian. In carrying out the integration over $\boldsymbol{\sigma}_{2n}$, it is convenient to introduce a mean field for the magnetic moment, i.e.,

$$H_\sigma^{(2n)} + H_{S\sigma}^{(2n)} = -\boldsymbol{\sigma}_{2n}\cdot\boldsymbol{B}_{2n} - K_\sigma^z\langle\sigma_{2n}^z\rangle^2 + K_\sigma^x\langle\sigma_{2n}^x\rangle^2, \tag{4}$$

with

$$\boldsymbol{B}_{2n} = -J(\boldsymbol{S}_{2n-1} + \boldsymbol{S}_{2n+1}) - 2K_\sigma^z\langle\sigma_{2n}^z\rangle\boldsymbol{e}_z + 2K_\sigma^x\langle\sigma_{2n}^x\rangle\boldsymbol{e}_x, \tag{5}$$

under the mean field approximation $(\sigma_{2n}^{x(z)} - \langle\sigma_{2n}^{x(z)}\rangle)^2 \simeq 0$, where $\boldsymbol{e}_{x(z)}$ represents the unit vector pointing in the $x(z)$ direction. Based on the calculations shown in the Appendix, we obtain the effective Hamiltonian H':

$$\begin{aligned}H' = -J'\sum_{\langle i,j\rangle}\boldsymbol{S}_i\cdot\boldsymbol{S}_j + \sum_i\Bigg[K_z'(S_i^z)^2 - K_x'(S_i^x)^2 \\ - \frac{K_S^{xy}}{4}\{(S_i^x)^2 - (S_i^y)^2\}^2\Bigg],\end{aligned} \tag{6}$$

where $\langle i,j\rangle$ represents the sum over the nearest neighbors only. The exchange ($J' > 0$) and anisotropy (K_x' and K_z') coefficients together with the conditions $J' > 0$, $K_z' \gg K_x'$, and $K_S^{xy} > 0$ are given, respectively, by

$$J' = \frac{J\sigma}{2S}, \tag{7}$$

$$K_x' = K_S^x - \frac{\sigma^2}{S^2}K_\sigma^x, \tag{8}$$

$$K_z' = K_S^z + \frac{\sigma^2}{S^2}K_\sigma^z. \tag{9}$$

This means that the ferrimagnetic-aligned nanoparticle chain indicated in Fig. 2(a) can be effectively considered as single-domain magnets with the same size magnetic moments aligned with a fixed space a, leading to the ferromagnetic-aligned nanoparticle chain as shown in Fig. 2(b). The magnetic moment vector $\boldsymbol{S}$ rotates in the xy plane due to the condition $K_z' \gg K_x', K_S^{xy}$.

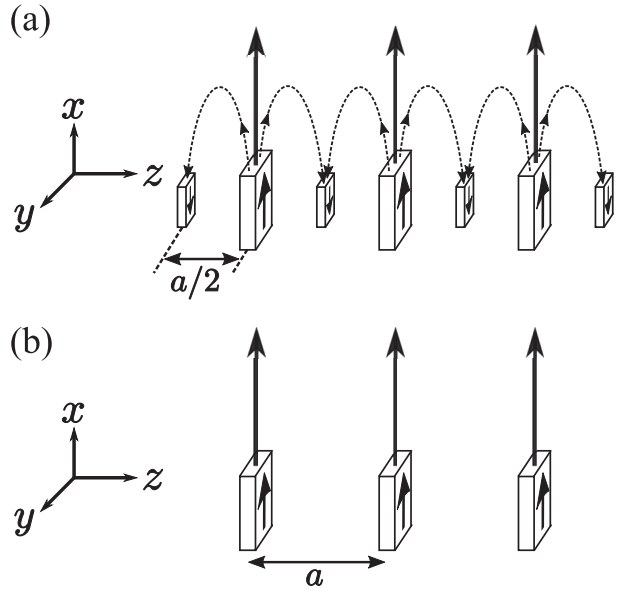

FIG. 2. (a) Ferrimagnetic-aligned nanoparticle chain. The nanoparticles of different sizes are aligned with fixed space $a/2$. The magnetic moments alternatively direct upward and downward for the energetical stability similar to the ferrimagnets. (b) The effective ferromagnetic-aligned nanoparticle chain, where the same size magnetic moments are aligned with fixed space a.

D. Magnetic solitons as a magnetic-field source

Now let us consider dynamics of magnetic moments in the effective ferromagnetic-aligned nanoparticle chain obtained above and derive two types of soliton solutions as a magnetic-field source. The effective magnetic field $\boldsymbol{B}_i$ generated by the magnetic moment $\boldsymbol{S}_i$ in the nanoparticles is given as

$$\boldsymbol{B}_i = -\frac{dH'}{d\boldsymbol{S}_i}. \tag{10}$$

This causes Larmor precession in magnetic moments [12]. The equation of motion is

$$\frac{d\boldsymbol{S}_i}{dt} = \boldsymbol{S}_i \times \boldsymbol{B}_i. \tag{11}$$

Under the continuum approximation, magnetic moments are expressed in spherical coordinates as follows:

$$\begin{aligned}\boldsymbol{S}_i &= \boldsymbol{S}(z) \\ &= S(\cos\delta\cos\phi(z), \cos\delta\sin\phi(z), \sin\delta),\end{aligned} \tag{12}$$

where ϕ is the azimuthal angle and $\delta(=\pi/2-\theta)$ is the perturbation angle with θ being the polar angle. The perturbation angle δ is assumed to be sufficiently small, so that $\sin\delta \simeq \delta$ and $\cos\delta \simeq 1$ hold. We also use the approximation $(\partial\phi/\partial z)^2 \simeq 0$. From Eq. (11), we obtain

$$\frac{\partial\delta}{\partial t} = J'Sa^2\frac{\partial^2\phi}{\partial z^2} - K'_xS\sin 2\phi - \frac{1}{2}K_S^{xy}S^3\sin 4\phi, \tag{13}$$

$$\begin{aligned}\frac{\partial\phi}{\partial t} &= 2K'_zS\delta + 2K'_xS\delta\cos^2\phi + K_S^{xy}S^3\delta\cos^2 2\phi \\ &\simeq 2K'_zS\delta,\end{aligned} \tag{14}$$

leading to double sine-Gordon equation

$$\frac{\partial^2\phi}{\partial t^2} - v_0^2\frac{\partial^2\phi}{\partial z^2} + m_1^2\sin 2\phi + m_2^2\sin 4\phi = 0, \tag{15}$$

where $v_0^2 = 2K'_zJ'S^2a^2$, $m_1^2 = 2K'_xK'_zS^2$, and $m_2^2 = K_S^{xy}K'_zS^4$. v_0 stands for the velocity of the linear wave. The double sine-Gordon equation has been investigated in detail and is known to have various types of soliton solutions depending on the parameters [17]. Here, let us focus on two types of solitons that are useful for the generation of black hole solitons to be discussed below.

E. 90-degree magnetic solitons

The first type of soliton is the 90-degree ($\perp$) magnetic soliton as shown in Fig. 3(a), which reproduces a *single* black hole equivalent to the black hole proposed by Nation *et al.* [8] except for the characteristics of the soliton. This soliton solution is obtained in the double sine-Gordon equation [Eq. (15)] when $m_1 = 0$, that is, the uniaxial coefficient K'_x is 0. The 90-degree magnetic soliton solution is expressed as

$$\phi^{\perp}(z,t) = \arctan\{e^{\pm(\gamma/d_0^{\perp})(z-v_st)}\}, \tag{16}$$

with the soliton velocity v_s, $d_0^{\perp} = a\sqrt{J'/4K_S^{xy}S^2}$, and Lorentz factor $\gamma = 1/\sqrt{1-(v_s/v_0)^2}$. Figure 3(a) shows the 90-degree magnetic soliton expressed by the soliton

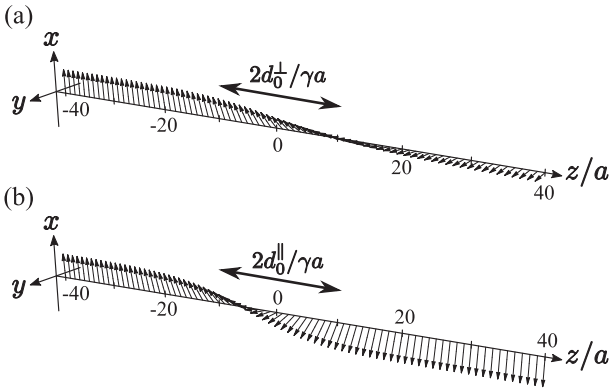

FIG. 3. Sketch of the soliton with the width $d \sim 2d_0^{\perp(\parallel)}/\gamma$ in the effective ferromagnetic-aligned nanoparticle chain, where nanoparticles are arranged at uniform distance a. z/a denotes the number of dc SQUIDs. (a) 90-degree magnetic soliton and (b) 180-degree magnetic soliton.

solution Eq. (16) with the width $d \sim 2d_0^{\perp}/\gamma$. The continuum approximation is applicable when the soliton width is larger than the unit length $d/a \sim \sqrt{J'/4K_S^{xy}S^2}/\gamma > 1$. This condition can be satisfied by properly designing the system parameters and soliton velocity. This type of soliton results from biaxial magnetic anisotropy with the anisotropy energy $-K_S^{xy}\{(S_i^x)^2 - (S_i^z)^2\}^2/4$ where the magnetization along $+x$ and $+y$ is degenerate. Therefore, the magnetic moments in the effective ferromagnetic-aligned nanoparticle chain are forced to rotate 90° for a transition between two equilibrium states.

F. 180-degree magnetic solitons

On the other hand, the 180-degree ($\parallel$) magnetic solitons are formed when $m_2 = 0$, equivalently, the biaxial magnetic anisotropy constant $K_S^{xy} = 0$. The soliton solution of Eq. (15) is similarly expressed as

$$\phi^{\parallel}(z,t) = 2\arctan\{e^{\pm(\gamma/d_0^{\parallel})(z-v_s t)}\}, \tag{17}$$

with $d_0^{\parallel} = a\sqrt{J'/2K_x'}$. Figure 3(b) shows the 180-degree magnetic soliton formed by the soliton solution Eq. (17) with the width $d \sim 2d_0^{\parallel}/\gamma$. In this case, the magnetization along $+x$ and $-x$ is degenerate due to the uniaxial magnetic anisotropy energy $-K_x'(S_i^x)^2$. The magnetic moments in the effective ferromagnetic-aligned nanoparticle chain are forced to rotate 180° for a transition between two equilibrium states. This is the origin of the 180-degree magnetic soliton generation. Unlike 90-degree magnetic solitons, the 180-degree magnetic solitons form black hole *pairs* as described below.

III. BLACK HOLE SOLITONS

Here, let us discuss black hole solitons generated using magnetic solitons. In the Josephson circuit, the kinetic inductance $L(\Phi)$ of the junction depends on the flux Φ through dc SQUID as follows:

$$L(\Phi) = \frac{L_0}{\cos(2\pi\Phi/\Phi_0)} \tag{18}$$

with magnetic flux quantum $\Phi_0 = h/2e$ and the Josephson inductance $L_0 = \hbar/2eI_c$. As is well known, the propagation velocity of electromagnetic wave c in this circuit is given by $c = a/\sqrt{LC}$. Thus, the propagation velocity depending on the magnetic flux through dc SQUID is expressed as

$$\bar{c}(\Phi) = \sqrt{\cos(2\pi\Phi/\Phi_0)}, \tag{19}$$

where c is normalized by $c_0 = a/\sqrt{L_0C}$. In our model, the magnetic field perpendicular to the SQUID is generated by the magnetic moments of the single-domain magnets chain. The magnetic flux threading through the dc SQUID with its area A is

$$\Phi = B_x A = \frac{SA}{2\pi l^3}\cos\phi = \frac{\Phi_1}{2\pi}\cos\phi \tag{20}$$

with $\Phi_1 = SA/l^3$. By substituting soliton solutions for the azimuthal angle ϕ of the magnetic moments, the magnetic flux is then obtained. The magnetic flux induced by the magnetic solitons modulates the velocity of an electromagnetic wave spatially as

$$\bar{c}(z,t) = \sqrt{\cos\{\bar{\Phi}\cos\phi(z,t)\}}, \tag{21}$$

where $\bar{\Phi} = \Phi_1/\Phi_0$, leading to the analog black holes.

There are three conditions for creating analog black holes in our system. First, the velocity of an electromagnetic wave in the circuit expressed in Eq. (21) must be real. This leads to the condition $0 \le \bar{\Phi} \le \pi/2$. Second, the soliton velocity is faster than the lower limit of the velocity of an electromagnetic wave in the circuit, i.e., $\lim_{z\to\pm\infty}\bar{c}(z,t) = \sqrt{\cos\bar{\Phi}} < \bar{v}_s$. The third is the natural condition that the velocity of an electromagnetic wave in the circuit under the magnetic field is slower than the velocity of an electromagnetic wave with no magnetic field. As a result, the soliton velocity is restricted in the range $\sqrt{\cos\bar{\Phi}} < \bar{v}_s < 1$.

In addition, we discuss the observability of the Hawking radiation in our system by deriving the Hawking temperature T_H analytically using the formula [18]

$$T_H = \frac{\hbar}{2\pi k_B}\left|\frac{\partial c}{\partial z}\right|_{z=z_h}, \tag{22}$$

where k_B is the Boltzmann constant. Note that this formula is applicable only under the continuum approximation $d > a$. Otherwise, a well-known trans-Planckian problem in general relativity occurs when the discreteness is pronounced [19–24]. The inter-SQUID distance a plays the role of the Planck length in this system, but this is beyond the scope of this paper.

A. Black hole solitons induced by the 90-degree magnetic solitons

Here, let us consider the black hole solitons induced by a 90-degree magnetic soliton obeying Eq. (16). The magnetic flux through the dc SQUID is written as

$$\begin{aligned}\Phi^{\perp}(z,t) &= \frac{\Phi_1}{2\pi}\cos\left[\arctan\{e^{\pm(\gamma/d_0^{\perp})(z-v_s t)}\}\right] \\ &= \frac{\Phi_1}{2\pi}\sqrt{\frac{1}{2}\{1 \mp \tanh(\gamma(z-v_s t)/d_0^{\perp})\}},\end{aligned} \tag{23}$$

by using Eq. (20). The magnetic flux through the dc SQUID in the transmission line changes spatially between 0 and $\Phi_1/2\pi$ as shown in Fig. 4(b), since the magnetic moments rotate 90° as shown in Fig. 4(a). From Eq. (18),

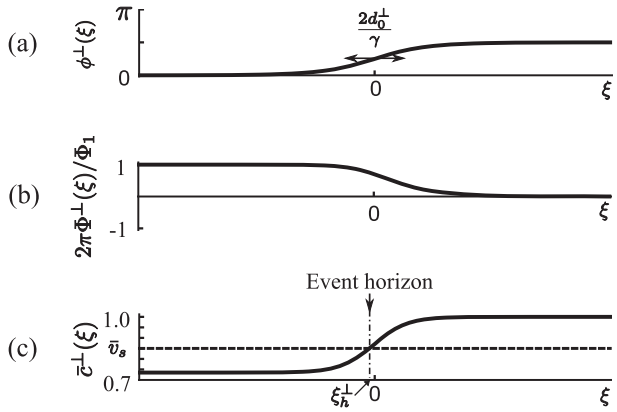

FIG. 4. (a) The rotation angle of the magnetic moments in the xy plane at ξ in the comoving frame. (b) The spatially varying magnetic flux applying to the dc-SQUID array in the comoving frame. (c) The normalized velocity of the electromagnetic wave with $\bar{\Phi} = 1$ in the comoving frame. The horizontal dotted line represents the normalized soliton velocity $\bar{v}_s = 0.98$. $\xi_h^{\perp}$ indicates the position of the event horizon.

one has the spatially varying Josephson inductance $L(\Phi)$ as follows:

$$L^{\perp}(\Phi) = \frac{L_0}{\cos\left[\bar{\Phi}\sqrt{\frac{1}{2}\{1 \mp \tanh(\gamma(z - v_s t)/d_0^{\perp})\}}\right]}. \quad (24)$$

As a result, the effective velocity of an electromagnetic wave in the dc-SQUID array transmission line is obtained from Eq. (19) as

$$\bar{c}^{\perp}(z,t) = \sqrt{\cos\left[\frac{\bar{\Phi}}{\sqrt{2}}\{1 \mp \tanh(\gamma(z - v_s t)/d_0^{\perp})\}^{1/2}\right]}. \quad (25)$$

Figure 4(c) shows the normalized space-dependent velocity of an electromagnetic wave in the comoving frame at $\bar{v}_s = 0.98$ as an example. The event horizon occurs at $(\bar{c}(\xi_h^{\perp}))^2 = \bar{v}_s^2$. The position of the event horizon in the comoving frame is given by

$$\xi_h^{\perp} = \pm\frac{d_0^{\perp}}{\gamma}\operatorname{arctanh}\left(\frac{2}{\bar{\Phi}^2}\arccos^2 \bar{v}_s^2 - 1\right) \quad (26)$$

and is shown in Fig. 5(b). An analog black hole can be formed where the velocity of the electromagnetic wave is slower than the soliton velocity.

Now, we derive the Hawking temperature in the obtained analog black hole. Substituting Eq. (25) into Eq. (22), we obtain the formula

$$T_H^{\perp} = (T_H^0)^{\perp} f^{\perp}(\bar{v}_s), \quad (27)$$

where $(T_H^0)^{\perp}$ and $f^{\perp}(\bar{v}_s)$ stand for *bare* Hawking temperature and soliton characteristic function, respectively, and are given as follows:

$$(T_H^0)^{\perp} = \frac{\hbar}{2\pi k_B} c_0 \frac{1}{d_0^{\perp}}, \quad (28)$$

$$f^{\perp}(\bar{v}_s) = \frac{1}{2}(\arccos \bar{v}_s^2)\sqrt{1 + \frac{1}{\bar{v}_s^2}}\left|1 - \left(\frac{\arccos \bar{v}_s^2}{\bar{\Phi}}\right)^2\right|. \quad (29)$$

The bare Hawking temperature $(T_H^0)^{\perp}$ given solely by the system parameters determines the rough temperature scale. Thus, one can control $(T_H^0)^{\perp}$ by designing the system parameters. For example, assuming $d \sim 2d_0^{\perp}/\gamma > a$ to satisfy the continuum approximation together with circuit parameters accessible with current technology, typically, $C \sim 10^{-16}F$ and $I_0 \sim 10^{-7}A$, the bare Hawking temperature T_H^0 is in the sub-Kelvin order and is fully observable.

In addition, it is found that the Hawking temperature also depends on the soliton velocity $\bar{v}_s$ as shown in Fig. 5(d), which was not found in previous studies. This is essentially due to the relativistic dynamical contribution of the soliton $f^{\perp}(\bar{v}_s)$ through the Lorentz factor as discussed below. According to Eq. (22), the Hawking temperature is determined by the velocity gradient of the electromagnetic wave in the circuit at the event horizon. The two elements of the definition, the velocity gradient and the position of the event horizon, both depend on the soliton velocity.

First, let us discuss the velocity gradient of the electromagnetic wave in the circuit, which is introduced by the magnetic soliton. The velocity gradient then depends on the soliton shape that is characterized by the soliton width $d \sim 2d_0^{\perp}/\gamma$. A short soliton width means a steep velocity

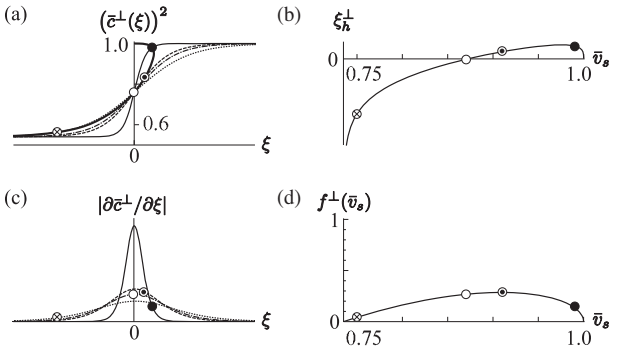

FIG. 5. (a) Spatial dependence of squared velocity of the electromagnetic wave $(\bar{c}^{\perp}(\xi))^2$ for some typical soliton velocities; $\bar{v}_s = 0.75$ (dotted line), 0.87 (one-dot chain line), 0.91 (dashed line), and 0.99 (solid line). The position of event horizons is depicted by the bold line with circles corresponding to the typical soliton velocities shown above, such as $\bar{v}_s = 0.75$ (cross inside circle), 0.86 (open circle), 0.91 (circled dot), and 0.99 (filled circle). The circles in all embedded figures correspond to these values. (b) The position of the event horizon as a function of the soliton velocity. (c) The velocity gradient of the electromagnetic wave $|\partial\bar{c}^{\perp}/\partial\xi|$. (d) The Hawking temperatures $f^{\perp}(\bar{v}_s)$ given in Eq. (29) under the condition $\bar{\Phi} = 1$ as a function of the soliton velocity $\bar{v}_s$.

gradient. The width contains the Lorentz factor γ depending on the soliton velocity. Thus, the soliton width decreases as the soliton velocity increases due to the Lorentz contraction. This makes the tanh-type soliton shape steeper. In other words, the relativistic effect γ increases the slope of the soliton, resulting in a steeper velocity gradient of the electromagnetic wave.

The second factor that affects the Hawking temperature, which involves the soliton velocity, is the position of the event horizon. Figure 5(b) shows the position of the event horizon as a function of the soliton velocity. This strange behavior is due to the peculiar soliton-velocity dependence on the Lorentz factor. As you can see in Fig. 5(a), when the soliton velocity increases, the position of the event horizon shifts to the right at first. This is simply because $\bar{c}^{\perp}(\xi_h^{\perp})$, which satisfies the event horizon condition, increases. Lorentz contractions are less important for slow solitons. However, it then turns to the left from a certain point. This is due to the Lorentz contraction manifested at a soliton velocity close to the speed of light. The soliton width becomes shorter, and the points that satisfy the condition shift to the left.

To summarize the above discussion, the Hawking temperature increases monotonically with increasing soliton velocity and decreases rapidly to zero at high velocities where Lorentz contraction becomes prominent. In these decreasing parts in temperature, the soliton width shortens rapidly and the velocity gradient $|\partial\bar{c}^{\perp}/\partial\xi|$ approaches the delta function. Therefore, the velocity gradient at the event horizon decreases rapidly and finally becomes 0. In other words, the change of the velocity gradient approaching the delta function is more rapid than the change of the position of the event horizon as a function of the soliton velocity.

B. Black hole solitons induced by the 180-degree magnetic solitons

Here, let us consider the black hole solitons created by the 180-degree magnetic soliton obtained in Eq. (17). The magnetic flux through the dc SQUID is written as

$$\Phi^{\parallel}(z,t) = \frac{\Phi_1}{2\pi}\cos\left[2\arctan\{e^{\pm(\gamma/d_0^{\parallel})(z-v_s t)}\}\right] = \frac{\Phi_1}{2\pi}\tanh\{\mp\gamma(z-v_s t)/d_0^{\parallel}\}, \tag{30}$$

by using Eq. (20). The magnetic flux through the dc SQUID in the transmission line changes spatially between $-\Phi_1/2\pi$ and $\Phi_1/2\pi$ as shown in Fig. 6(b), since the magnetic moments rotate 180° shown in Fig. 6(a). From Eq. (18), the Josephson inductance is given as

$$L^{\parallel}(\Phi) = \frac{L_0}{\cos\left[\bar{\Phi}\tanh\{\mp\gamma(z-v_s t)/d_0^{\parallel}\}\right]}. \tag{31}$$

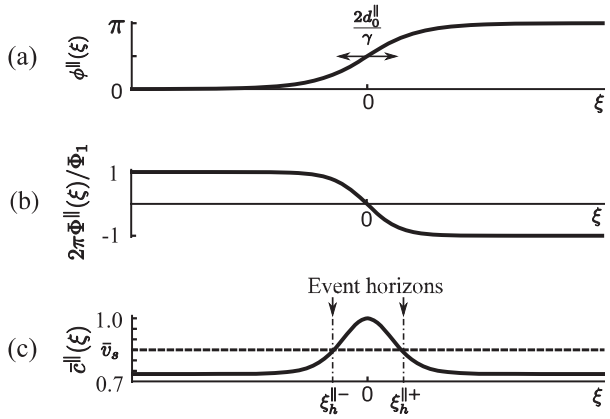

FIG. 6. (a) The rotation angle of the magnetic moments in the xy plane at ξ in the comoving frame. (b) The spatially varying magnetic flux applying to the dc-SQUID array in the comoving frame. (c) The normalized velocity of the electromagnetic wave with $\bar{\Phi} = 1$ in the comoving frame. The horizontal dotted line represents the normalized soliton velocity $\bar{v}_s = 0.98$. $\xi_h^{\parallel -}$ and $\xi_h^{\parallel +}$ indicate the black hole and white hole horizon positions, respectively.

The effective velocity of an electromagnetic wave in the transmission line is then obtained from Eq. (19) as

$$\bar{c}^{\parallel}(z,t) = \sqrt{\cos\left[\bar{\Phi}\tanh\{\mp\gamma(z-v_s t)/d_0^{\parallel}\}\right]}. \tag{32}$$

Figure 6(c) shows the normalized space-dependent velocity of electromagnetic wave in the comoving frame at $\bar{v}_s = 0.98$ similar to the example at the 90-degree soliton. The event horizon occurs at $(\bar{c}(\xi_h^{\parallel}))^2 = \bar{v}_s^2$. The position of the event horizon in the comoving frame is given by

$$\xi_h^{\parallel\pm} = \pm\frac{d_0^{\parallel}}{\gamma}\operatorname{arctanh}\left(\frac{1}{\bar{\Phi}}\arccos\bar{v}_s^2\right) \tag{33}$$

[see Fig. 7(b)]. Unlike the analog black hole induced by 90-degree magnetic solitons, *the pair of analog black holes* can be created where the velocity of the electromagnetic wave is slower than the soliton velocity.

Here, we discuss the observability of the Hawking radiation in the pair of the analog black holes by deriving the Hawking temperature analytically using Eq. (22). The Hawking temperature is expressed as

$$T_H^{\parallel} = (T_H^0)^{\parallel} f^{\parallel}(\bar{v}_s), \tag{34}$$

where $(T_H^0)^{\parallel}$ and $f^{\parallel}(\bar{v}_s)$ represent the bare Hawking temperature and the soliton characteristic function, respectively, and are written as follows:

$$(T_H^0)^{\parallel} = \frac{\hbar}{2\pi k_B}c_0\bar{\Phi}\frac{1}{d_0^{\parallel}}, \tag{35}$$

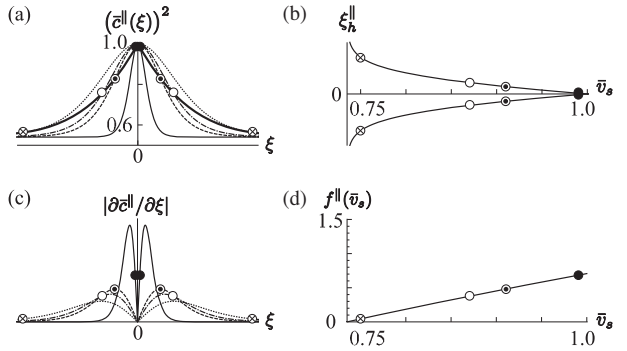

FIG. 7. (a) Spatial dependence of squared velocity of the electromagnetic wave $(\bar{c}^{\parallel}(\xi))^2$ for some typical soliton velocities; $\bar{v}_s = 0.75$ (dotted line), 0.87 (one-dot chain line), 0.91 (dashed line), and 0.99 (solid line). The pair of event horizons are formed for each soliton velocities unlike 90-degree magnetic solitons. The position of event horizons is depicted by the bold line with circles corresponding to the typical soliton velocities shown above, such as $\bar{v}_s = 0.75$ (cross inside circle), 0.86 (open circle), 0.91 (circled dot), and 0.99 (filled circle). The circles in all embedded figures correspond to these values. (b) The position of the event horizon as a function of the soliton velocity. (c) The velocity gradient of the electromagnetic wave $|\partial\bar{c}^{\parallel}/\partial\xi|$. It is symmetric about the vertical axis so that the Hawking temperatures are the same at both positions of the event horizons. (d) The Hawking temperatures $f^{\parallel}(\bar{v}_s)$ given in Eq. (36) under the condition $\bar{\Phi} = 1$ as a function of the soliton velocity $\bar{v}_s$.

$$f^{\parallel}(\bar{v}_s) = \frac{1}{2}\sqrt{1+\frac{1}{\bar{v}_s^2}}\left|1-\left(\frac{\arccos\bar{v}_s^2}{\bar{\Phi}}\right)^2\right|. \tag{36}$$

The bare Hawking temperature $(T_H^0)^{\parallel}$ determines the rough temperature scale. One can control $(T_H^0)^{\parallel}$ by designing the system parameters, since it depends solely on the system parameters. For example, assuming $d \sim 2d_0^{\parallel}/\gamma > a$ at $\bar{\Phi} = 1$ together with circuit parameters accessible with current technology, the bare Hawking temperature T_H^0 is in the sub-Kelvin order and is also observable.

Similar to the black hole soliton formed by the 90-degree magnetic solitons, the Hawking temperature is also found to be dependent on the soliton velocity $\bar{v}_s$ as shown in Fig. 7(d), which has not been found in the previous studies. This is due to the same relativistic mechanism as the black hole soliton induced by 90-degree magnetic solitons. Here, only the differences are described. The velocity of the electromagnetic wave in the circuit is symmetric with respect to the origin. This is the origin of two degenerate event horizons. Therefore, the soliton-velocity dependence is the same for two event horizons. In fact, the soliton-velocity dependence on the Hawking temperature is exactly the same for black holes and white holes as shown in Fig. 7(d).

To summarize our black hole solitons, their Hawking temperatures reflect the dynamic properties of soliton and show unprecedented properties that depend on the soliton velocity. This dependence implies that the Hawking temperature can be controlled simply by changing the soliton velocity without changing the circuit configuration at all. Therefore, this change confirms that the experimentally detected radiation is actually due to Hawking radiation. This is an excellent advantage that has never been seen before.

IV. SUMMARY

We have investigated analog black holes generated in an array of dc SQUIDs coupled in parallel with a one-dimensional chain of single-domain nanomagnets. Starting with a ferrimagnetic-aligned nanoparticle chain with alternating magnetic moments in both direction and magnitude, we have shown that the ferrimagnetic-aligned nanoparticle chain can be effectively reduced to a ferromagnetic-aligned nanoparticle chain. Then, we derived two types of solitons that appear there. The magnetic solitons in the chain produce magnetic fields perpendicular to the SQUID array, leading to the spatially varying velocities of electromagnetic waves through the nonlinear inductance in the array. The effective event horizon is established where the soliton velocity is equal to the spatially varying velocity of the electromagnetic wave in the circuit. Therefore, an analog black hole is created in the region of the circuit with an effective velocity of the electromagnetic wave lower than the soliton velocity. It was found that 90-degree magnetic solitons produce single analog black holes as described in previous studies, whereas 180-degree magnetic solitons produce analog black hole pairs.

We have also derived the Hawking temperature in these analog black holes based on the tunneling mechanism for Hawking radiation. In our system, the electromagnetic wave produced by the quantum fluctuation of the Josephson phase near the classical soliton is observed as the Hawking radiation. According to the formula, Hawking radiation is observable in the circuit using existing technologies. In addition, the Hawking temperature reflects the characteristics of solitons, because the black holes are derived from solitons. That is, it depends on the soliton velocity. If this dependence can be confirmed experimentally, it can be identified that the observed radiation is certainly from an analog black hole. This might reinforce the previously known identification method based on the entanglement of radiated light [25].

ACKNOWLEDGMENTS

We thank N. S. N. S. Bahri for valuable discussions.

APPENDIX: DERIVATION OF THE EFFECTIVE FERROMAGNETIC HAMILTONIAN

Here, we derive the effective ferromagnetic Hamiltonian starting from our original ferrimagnetic Hamiltonian for a single-domain ferrimagnetic chain given in Eq. (1), which

is rewritten as

$$H = \sum_n (H_{S\sigma}^{(2n)} + H_S^{(2n)} + H_\sigma^{(2n)}), \tag{A1}$$

where

$$H_{S\sigma}^{(2n)} = J(\boldsymbol{S}_{2n-1}\cdot\boldsymbol{\sigma}_{2n} + \boldsymbol{\sigma}_{2n}\cdot\boldsymbol{S}_{2n+1}), \tag{A2}$$

$$H_S^{(2n)} = K_S^z (S_{2n-1}^z)^2 - K_S^x (S_{2n-1}^x)^2 - \frac{K_S^{xy}}{4}\{(S_{2n-1}^x)^2 - (S_{2n-1}^y)^2\}^2, \tag{A3}$$

$$H_\sigma^{(2n)} = K_\sigma^z (\sigma_{2n}^z)^2 - K_\sigma^x (\sigma_{2n}^x)^2. \tag{A4}$$

In order to remove the variables $\boldsymbol{\sigma}_{2n}$ from this Hamiltonian, let us consider the integration over $\boldsymbol{\sigma}_{2n}$ of the partition function as follows:

$$Z^{(2n)} = Z_S^{(2n)} \cdot Z_{\sigma,S\sigma}^{(2n)}, \tag{A5}$$

where

$$Z_S^{(2n)} = \exp(-\beta H_S^{(2n)}) \tag{A6}$$

$$Z_{\sigma,S\sigma}^{(2n)} = \int d\boldsymbol{\sigma}_{2n} \exp\{-\beta(H_\sigma^{(2n)} + H_{S\sigma}^{(2n)})\}. \tag{A7}$$

Equation (4) is derived by substituting Eq. (A8) for Eq. (A4) with $(\sigma_{2n}^{x(z)} - \langle\sigma_{2n}^{x(z)}\rangle)^2 \simeq 0$:

$$(\sigma_{2n}^{x(z)})^2 = (\sigma_{2n}^{x(z)} - \langle\sigma_{2n}^{x(z)}\rangle + \langle\sigma_{2n}^{x(z)}\rangle)^2 \simeq 2(\sigma_{2n}^{x(z)} - \langle\sigma_{2n}^{x(z)}\rangle)\langle\sigma_{2n}^{x(z)}\rangle + \langle\sigma_{2n}^{x(z)}\rangle^2. \tag{A8}$$

Then, we obtain

$$Z_{\sigma,S\sigma}^{(2n)} = \int d\boldsymbol{\sigma}_{2n} \exp\{-\beta(-\boldsymbol{\sigma}_{2n}\cdot\boldsymbol{B}_{2n} - K_\sigma^z\langle\sigma_{2n}^z\rangle^2 + K_\sigma^x\langle\sigma_{2_n}^x\rangle^2)\}. \tag{A9}$$

In order to carry out the integration over $\boldsymbol{\sigma}_{2n}$ in Eq. (A9), we use the polar variables with the azimuthal angle ϕ and the angle Θ between $\boldsymbol{\sigma}_{2n}$ and $\boldsymbol{B}_{2n}$ as follows:

$$Z_{\sigma,S\sigma}^{(2n)} = \int_0^{2\pi}\int_{-1}^{1} \exp[-\beta(-\sigma|\boldsymbol{B}_{2n}|\cos\Theta - K_\sigma^z\langle\sigma_{2n}^z\rangle^2 + K_\sigma^x\langle\sigma_{2n}^x\rangle^2)]d(\cos\Theta)d\phi \tag{A10}$$

$$= 2\pi\exp[-\beta(-K_\sigma^z\langle\sigma_{2n}^z\rangle^2 + K_\sigma^x\langle\sigma_{2n}^x\rangle^2)] \times \int_{-1}^{1}\exp[\beta\sigma|\boldsymbol{B}_{2n}|\cos\Theta]d(\cos\Theta) \tag{A11}$$

$$= \frac{2\pi}{\beta\sigma|\boldsymbol{B}_{2n}|}\exp[-\beta(-K_\sigma^z\langle\sigma_{2n}^z\rangle^2 + K_\sigma^x\langle\sigma_{2n}^x\rangle^2)] \times (\exp[\beta\sigma|\boldsymbol{B}_{2n}|] - \exp[-\beta\sigma|\boldsymbol{B}_{2n}|]). \tag{A12}$$

In the limit $\beta \to 0$, $Z_{\sigma,S\sigma}^{(2n)}$ converges as follows:

$$Z_{\sigma,S\sigma}^{(2n)} \to \frac{2\pi}{\beta\sigma|\boldsymbol{B}_{2n}|}\exp[-\beta(-K_\sigma^z\langle\sigma_{2n}^z\rangle^2 + K_\sigma^x\langle\sigma_{2n}^x\rangle^2)] \times \exp[\beta\sigma|\boldsymbol{B}_{2n}|] \tag{A13}$$

$$\sim \exp[-\beta(-\sigma|\boldsymbol{B}_{2n}| - K_\sigma^z\langle\sigma_{2n}^z\rangle^2 + K_\sigma^x\langle\sigma_{2n}^x\rangle^2)]. \tag{A14}$$

From Eq. (A5), we obtain

$$Z^{(2n)} \sim \exp[-\beta(H_S^{(2n)} - \sigma|\boldsymbol{B}_{2n}| - K_\sigma^z\langle\sigma_{2n}^z\rangle^2 + K_\sigma^x\langle\sigma_{2n}^x\rangle^2)]. \tag{A15}$$

In comparison with the right-hand side of Eq. (2), the effective Hamiltonian is given as

$$H'^{(2n)} \sim H_S^{(2n)} - \sigma|\boldsymbol{B}_{2n}| - K_\sigma^z\langle\sigma_{2n}^z\rangle^2 + K_\sigma^x\langle\sigma_{2n}^x\rangle^2. \tag{A16}$$

Now let us derive $|\boldsymbol{B}_{2n}|$ from Eq. (5) as follows:

$$\begin{aligned}
|\boldsymbol{B}_{2n}|^2 &= J^2(\boldsymbol{S}_{2n-1} + \boldsymbol{S}_{2n+1})^2 + 4(K_\sigma^z)^2\langle\sigma_{2n}^z\rangle^2\boldsymbol{e}_z^2 + 4(K_\sigma^x)^2\langle\sigma_{2n}^x\rangle^2\boldsymbol{e}_x^2 + 4JK_\sigma^z(\boldsymbol{S}_{2n-1} + \boldsymbol{S}_{2n+1})\langle\sigma_{2n}^z\rangle\boldsymbol{e}_z \\
&\quad - 4JK_\sigma^x(\boldsymbol{S}_{2n-1} + \boldsymbol{S}_{2n+1})\langle\sigma_{2n}^x\rangle\boldsymbol{e}_x - 4K_\sigma^xK_\sigma^z\langle\sigma_{2n}^x\rangle\langle\sigma_{2n}^z\rangle\boldsymbol{e}_z\cdot\boldsymbol{e}_x \\
&= 4J^2S^2 - J^2(\boldsymbol{S}_{2n-1} - \boldsymbol{S}_{2n+1})^2 + 4(K_\sigma^z)^2\langle\sigma_{2n}^z\rangle^2 + 4(K_\sigma^x)^2\langle\sigma_{2n}^x\rangle^2 + 4JK_\sigma^z(S_{2n-1}^z + S_{2n+1}^z)\langle\sigma_{2n}^z\rangle \\
&\quad - 4JK_\sigma^x(S_{2n-1}^x + S_{2n+1}^x)\langle\sigma_{2n}^x\rangle \\
&\simeq 4J^2S^2 - J^2(\boldsymbol{S}_{2n-1} - \boldsymbol{S}_{2n+1})^2 + 4JK_\sigma^z(S_{2n-1}^z + S_{2n+1}^z)\langle\sigma_{2n}^z\rangle - 4JK_\sigma^x(S_{2n-1}^x + S_{2n+1}^x)\langle\sigma_{2n}^x\rangle \\
&= 4J^2S^2\left\{1 - \frac{1}{4S^2}(\boldsymbol{S}_{2n-1} - \boldsymbol{S}_{2n+1})^2 + \frac{K_\sigma^z}{JS^2}\langle\sigma_{2n}^z\rangle(S_{2n-1}^z + S_{2n+1}^z) - \frac{K_\sigma^x}{JS^2}\langle\sigma_{2n}^x\rangle(S_{2n-1}^x + S_{2n+1}^x)\right\},
\end{aligned} \tag{A17}$$

where we use the approximation $4(K_\sigma^z)^2\langle\sigma_{2n}^z\rangle^2 + 4(K_\sigma^x)^2\langle\sigma_{2n}^x\rangle^2 \ll J^2S^2$. This leads to

$$|\boldsymbol{B}_{2n}| \simeq 2JS\Bigg\{1 - \frac{1}{8S^2}(\boldsymbol{S}_{2n-1} - \boldsymbol{S}_{2n+1})^2 - \frac{K_\sigma^z}{2JS^2}\langle\sigma_{2n}^z\rangle(S_{2n-1}^z + S_{2n+1}^z) + \frac{K_\sigma^x}{2JS^2}\langle\sigma_{2n}^x\rangle(S_{2n-1}^x + S_{2n+1}^x)\Bigg\}, \tag{A18}$$

by applying the approximation $\sqrt{1+x} \simeq 1 + x/2$ for small x. We obtain

$$Z_{\sigma,S\sigma}^{(2n)} \sim \exp\Bigg[-\beta\Bigg\{-2JS\sigma + \frac{J\sigma}{4S}(\boldsymbol{S}_{2n-1} - \boldsymbol{S}_{2n+1})^2 + \frac{\sigma K_\sigma^x}{S}\langle\sigma_{2n}^2\rangle(S_{2n-1}^x + S_{2n+1}^x) - \frac{\sigma K_\sigma^z}{S}\langle\sigma_{2n}^2\rangle(S_{2n-1}^z + S_{2n+1}^z) - K_\sigma^z\langle\sigma_{2n}^z\rangle^2 + K_\sigma^x\langle\sigma_{2n}^x\rangle^2\Bigg\}\Bigg] \tag{A19}$$

by substituting Eq. (A18) into Eq. (A14). The quantity $\langle\sigma_{2n}^x\rangle$ is obtained in self-consistent calculations using the following relation:

$$\langle\sigma_{2n}^x\rangle^2 = \frac{1}{\beta}\frac{\partial}{\partial K_\sigma^x}\ln Z_{\sigma,S\sigma}^{(2n)}, \tag{A20}$$

that holds from Eq. (A9). In addition, Eq. (A19) leads to the relation as follows:

$$\frac{1}{\beta}\frac{\partial}{\partial K_\sigma^x}\ln Z_{\sigma,S\sigma}^{(2n)} \sim -\frac{\sigma}{S}\langle\sigma_{2n}^2\rangle(S_{2n-1}^x + S_{2n+1}^x) - \langle\sigma_{2n}^x\rangle^2. \tag{A21}$$

These relations result in

$$\langle\sigma_{2n}^x\rangle^2 = -\frac{\sigma}{S}\langle\sigma_{2n}^x\rangle(S_{2n-1}^x + S_{2n+1}^x) - \langle\sigma_{2n}^x\rangle^2, \tag{A22}$$

$$\langle\sigma_{2n}^x\rangle = -\frac{\sigma}{2S}(S_{2n-1}^x + S_{2n+1}^x). \tag{A23}$$

We also obtain

$$\langle\sigma_{2n}^z\rangle = -\frac{\sigma}{S}(S_{2n-1}^z + S_{2n+1}^z), \tag{A24}$$

through procedures parallel to those described above.

Finally, we reach the effective Hamiltonian by substituting Eqs. (A18), (A23), and (A24) into Eq. (A16) as follows:

$$H'^{(2n)} \sim H_S^{(2n)} - 2JS\sigma + \frac{J\sigma}{4S}(\boldsymbol{S}_{2n-1} - \boldsymbol{S}_{2n+1})^2 + \frac{\sigma^2 K_\sigma^z}{4S^2}(S_{2n-1}^z + S_{2n+1}^z)^2 - \frac{\sigma^2 K_\sigma^x}{4S^2}(S_{2n-1}^x + S_{2n+1}^x)^2 \tag{A25}$$

$$\sim H_S^{(2n)} - \frac{J\sigma}{2S}\boldsymbol{S}_{2n-1}\cdot\boldsymbol{S}_{2n+1} + \frac{\sigma^2}{S^2}K_\sigma^z(S_{2n-1}^z)^2 - \frac{\sigma^2}{S^2}K_\sigma^x(S_{2n-1}^x)^2, \tag{A26}$$

where $S_{2n-1}^{x(z)} \simeq S_{2n+1}^{x(z)}$. The total effective ferromagnetic Hamiltonian for a ferrimagnetic-aligned nanoparticle chain is shown in Eq. (6).

[1] S. W. Hawking, Commun. Math. Phys. **43**, 199 (1975).
[2] J. B. Hartle and S. W. Hawking, Phys. Rev. D **13**, 2188 (1976).
[3] W. G. Unruh, Phys. Rev. Lett. **46**, 1351 (1981).
[4] T. A. Jacobson and G. E. Volovik, Phys. Rev. D **58**, 064021 (1998).
[5] T. G. Philbin, C. Kuklewicz, S. Robertson, S. Hill, F. König, and U. Leonhardt, Science **319**, 1367 (2008).
[6] L. J. Garay, J. R. Anglin, J. I. Cirac, and P. Zoller, Phys. Rev. Lett. **85**, 4643 (2000).
[7] R. Schützhold and W. G. Unruh, Phys. Rev. Lett. **95**, 031301 (2005).
[8] P. D. Nation, M. P. Blencowe, A. J. Rimberg, and E. Buks, Phys. Rev. Lett. **103**, 087004 (2009).
[9] J. S. Russell, Report of the Fourteenth Meeting of the British Association for the Advancement of Science, York, 311 (1844).
[10] N. J. Zabusky and M. D. Kruskal, Phys. Rev. Lett. **15**, 240 (1965).
[11] C. S. Gardner, J. M. Greene, M. D. Kruskal, and R. M. Miura, Phys. Rev. Lett. **19**, 1095 (1967).
[12] H. How, R. C. O'Handley, and F. R. Morgenthaler, Phys. Rev. B **40**, 4808 (1989).
[13] G.-P. Zheng, J.-Q. Liang, and W. M. Liu, Phys. Rev. B **79**, 014415 (2009).
[14] S. Ishizaka and K. Nakamura, J. Magn. Magn. Mater. **210**, 15 (2000).
[15] S. T. Chui and V. N. Ryzhov, Phys. Rev. Lett. **78**, 2224 (1997).

[16] F. Ferraro, D. Gatteschi, A. Rettori, and M. Corti, Mol. Phys. **85**, 1073 (1995).
[17] C. A. Condat, R. A. Guyer, and M. D. Miller, Phys. Rev. B **27**, 474 (1983).
[18] H. Katayama, N. Hatakenaka, and T. Fujii, Phys. Rev. D **102**, 086018 (2020).
[19] S. Corley, Phys. Rev. D **55**, 6155 (1997).
[20] S. Corley, Phys. Rev. D **57**, 6280 (1998).
[21] S. Corley and T. Jacobson, Phys. Rev. D **59**, 124011 (1999).
[22] W. G. Unruh, Phys. Rev. D **51**, 2827 (1995).
[23] U. Leonhardt, T. Kiss, and P. Öhberg, Phys. Rev. A **67**, 033602 (2003).
[24] V. Fleurov and R. Schilling, Phys. Rev. A **85**, 045602 (2012).
[25] J. Steinhauer, Nat. Phys. **12**, 959 (2016).